

Ground motions variability in Israel from 3-D simulations of M 6 and M 7 earthquakes

Jonatan Glehman¹ and Michael Tsesarsky^{1,2}

¹Department of Earth and Environmental Sciences, Ben Gurion University of the Negev, 8410501, Israel

²Department of Civil and Environmental Engineering, Ben Gurion University of the Negev, 8410501, Israel

Correspondence to: Jonatan Glehman (glehman@post.bgu.ac.il)

Abstract. In Israel, due to low seismicity rates and sparse seismic network, the temporal and spatial coverage of ground motion data is insufficient to estimate the variability of moderate-strong ($M > 6$) ground motions required to construct a local ground motion model (GMM). To fill this data gap and to study the ground motions variability of $M > 6$ events, we performed a series of 3-D numerical simulations of M 6 and M 7 earthquakes. Based on the results of the simulations, we developed a parametric attenuation model (AM) and studied the residuals between simulated and AM PGVs and the single station variability. We also compared the simulated ground motions with a global GMM in terms of peak ground velocity (PGV) and significant duration (D_s 595). Our results suggested that the AM was unable to fully capture the simulated ground motions variability, mainly due to the incorporation of super-shear rupture and effects of local sedimentary structures. We also showed that an imported GMM considerably deviates from simulated ground motions. This work sets the basis for future development of a comprehensive GMM for Israel, accounting for local sources, path, and site effects.

1 Introduction

The recent report by the Centre for Research on the Epidemiology of Disasters (CRED) and the UN Office for Disaster Risk Reduction (UNDRR) – Human Cost of Disasters, 2000 - 2019 – clearly shows that earthquakes are the deadliest natural disasters. Accounting for only 3 % of the total number of people affected by natural disasters, they count for 58 % of deaths (more than 700,000) of all disaster types and 21 % of recorded economic losses (Mizutori and D’ebarati, 2020). Over the past 40 years, the global population exposed to a moderate to severe intensity earthquake has increased by 93 % (to 2.7 billion people) (Pesaresi et al., 2017). This value is expected to grow with population growth and increasing urbanization.

Seismic hazard is the intrinsic natural occurrence of earthquakes and the resulting ground motion and other effects (Wang, 2005). Ground motion models (GMM’s) are critical components in the mitigation of seismic hazard. Empirically based GMMs, also known as Ground Motion Prediction Equations (GMPE’s), are parametric models that estimate the median and the variability of the expected ground motions at a site. The main explanatory variables of such models are typically earthquake magnitude, distance, and site conditions. New generation GMMs also address faulting style, depth to rock, and others.

Many regions worldwide, either due to low seismicity rates and/or sparse coverage of the seismic network, do not provide sufficient temporal and spatial data to estimate the variability of ground motions required to construct a local GMM or validate an imported GMM to local conditions. This situation is specifically acute in the range of strong earthquakes at relatively short distances that pose the most significant hazard to human life and infrastructure.

37 The use of imported GMM's under the ergodic assumption attributes the ground motion variability to the
38 randomness of the process (i.e., aleatory variability) rather than to local systematic source-path and site effects
39 (i.e., epistemic uncertainty) (Anderson and Brune, 1999). Abrahamson et al., (2019) showed that the increased
40 number of strong-motion records over the past decade exhibit significant differences in scaling of the ground
41 motions even within relatively small regions and that most of the variability typically treated as aleatory is actually
42 due to systematic source, path, and site effects. Kuehn et al., (2019) showed the importance of variations in quality
43 factor (Q) over small spatial scales (30 km) in California. Specifically showing that accounting for path effects
44 leads to a smaller value of the aleatory variability and results in different median predictions, depending on source
45 and site location. To achieve this improvement, Kuehn et al., (2019) divided California into a grid with a cell size
46 of 30 km by 30 km and used 12,039 records from 274 events recorded at 1504 stations. This approach can be
47 employed only in data-rich regions, such as California. Lan et al., (2019) showed that for South Western China,
48 imported GMM's result in significant discrepancies compared with regional instrumental data (including the
49 Wenchuan Mw 7.9 event). In addition, despite the recorded ground motion data expanding, it remains sparse for
50 large, complex ruptures with recurrence intervals generally exceeding the observation length of instrumental
51 records.

52 The challenges met while predicting ground motion in data-poor regions turn numerical modeling into an
53 essential complementary method for seismic hazard analysis (Chaljub et al., 2010). Numerical modeling alleviates
54 the need for the ergodic assumption, as it can augment the seismic data with strong motion records and account
55 for ground motions variability by systematically separating source, path, and site effects. For example, Graves et
56 al., (2011) showed that the combination of rupture directivity and basin response effects could lead to an increased
57 hazard in particular sites, relative to that calculated by GMM. Pitarka et al., (2021) found that the combination of
58 rupture propagation effects with the amplification due to local topography can result in large ground motions
59 amplifications with complex spatial variability.

60 However, the shift from ergodic models to nonergodic models, which account for local source-site and
61 path effects such as numerical models, leads to large epistemic uncertainty in the median ground motion, resulting
62 in increased epistemic uncertainty of the hazard (Walling and Abrahamson, 2012). Such uncertainty is derived
63 from both modeling and parametric uncertainties, as the model, is not well constrained. Model uncertainty can be
64 reduced by using more accurate 3D crustal models and source models.

65 Subsurface models with different levels of accuracy and completeness are available around the world. With
66 the increasing use of terrestrial and space geodesy, the control of seismic sources is also improving with time.
67 Combining the two enables the construction of numerical models for regional assessment of ground motions
68 (Pitarka et al., 2021; Douglas and Aochi, 2008; Graves and Pitarka, 2015). A hybrid GMM, based on empirical
69 and synthetic ground motion databases, is expected to reduce the epistemic uncertainty of the median ground
70 motion and will lead to a lower aleatory variability than GMM's based on data with limited magnitude and distance
71 bands.

72 In Israel, low seismicity rates (centennial and millennial return periods) and a limited instrumental catalog,
73 spanning only four decades and contain mainly $M < 6$ events, impede the development of local empirical GMM.
74 The practical outcome of this shortcoming is the use of imported GMM's, such as the Campbell & Bozorgnia,
75 (2008; hereafter, CB08) used in the Israel Seismic Design Code IS 413 (Israel Standards Institution, 2013).

76 Contrary to the instrumental catalog, the Israel pre-instrumental catalog spans over three millennia (Agnon, 2014),
77 including numerous $M > 6$ events, with up to 14 $M > 7$ events.

78 This paper presents numerical modeling of ground motions in Israel, intended to study ground motions
79 variability from moderate ($M 6$) and strong ($M 7$) earthquakes. The primary purpose of this work was to study the
80 different source, path, and site effects of simulated $M 6$ and $M 7$ earthquakes and their contribution to ground
81 motion variability in Israel. To this end, we have improved the 3-D regional velocity model of Shimony et al.,
82 (2021) and numerically modeled $M 6$ and $M 7$ earthquakes with different source and path properties. Following,
83 we developed a parametric model of median ground motions and their variability in terms of Peak Ground
84 Velocity (PGV). The model quantifies the spatial distribution of the ground motions in central and northern Israel,
85 accounting for source, path, and site effects.

86 We begin with a brief introduction to the seismo-tectonic setting of the region. Then, we proceed to the
87 methodology section to describe the process of generating a synthetic ground motion database and the subsequent
88 construction of a parametric ground motion model. Next, in the results section, we present the simulated ground
89 motions and the respective attenuation model. Then, we show the comparison between the results of our
90 simulations and global GMM's of Campbell & Bozorgnia, (2014; hereafter, CB14) and Afshari & Stewart, (2016).
91 Finally, we discuss our findings and provide insights regarding the seismic hazard from moderate to strong
92 earthquakes and the importance of developing a regional GMM to mitigate the seismic hazard in Israel.

93 **2 The seismo-tectonic setting of Israel**

94 **2.1 Seismicity and seismic hazard in Israel**

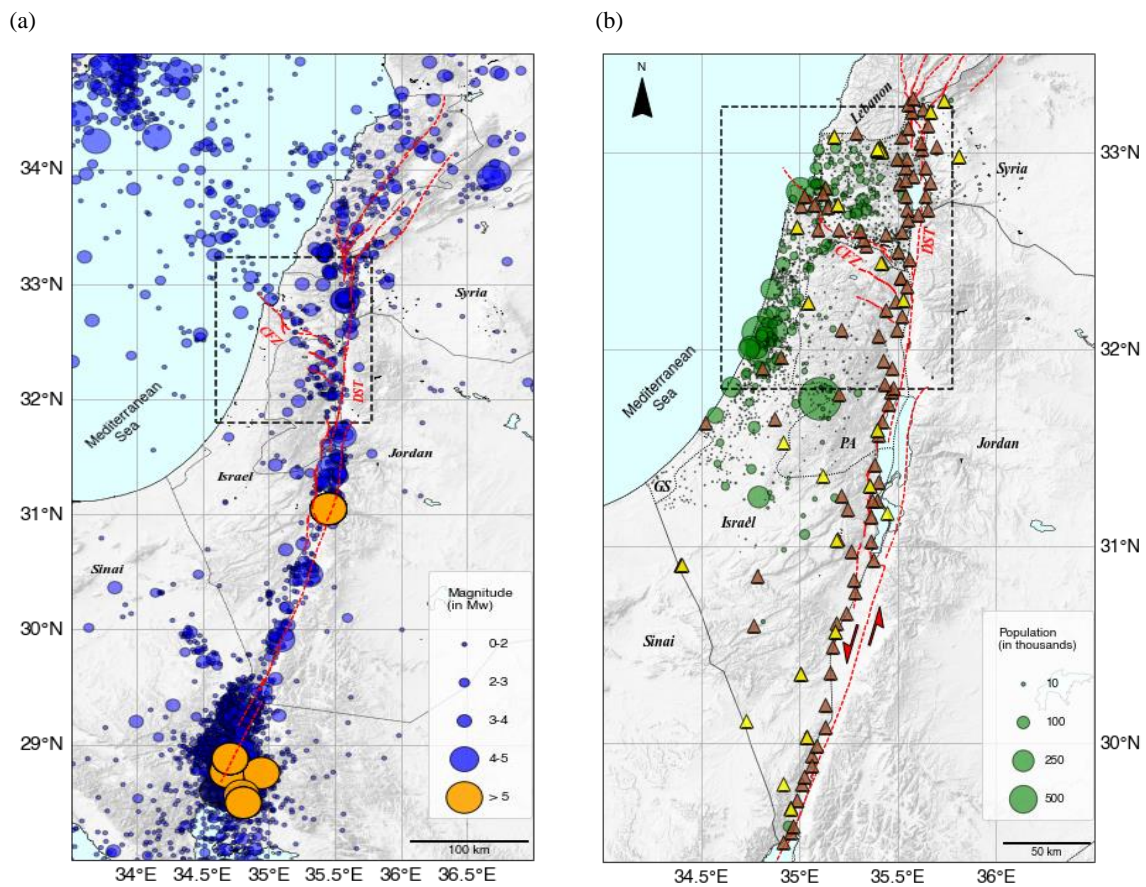
95 The Dead Sea Transform (DST) fault system is an active tectonic boundary separating the African and Arabian
96 plates. Extending from the Gulf of Aqaba to southern Turkey, a total length of approx. 1100 km, it dominates the
97 seismicity of Israel, Palestinian Authority, Lebanon, and Syria (Fig. 1a,b). The DST is a left-lateral strike-slip
98 fault with a total offset of 105 km (Garfunkel, 2014). The average long-term slip rate is 4 to 5 mm year⁻¹ (Bartov
99 et al., 1980). Geodetic slip rates along the Israeli part of the DST range from 3 to 5 mm year⁻¹ (Hamiel et al., 2016;
100 Sadeh et al., 2012).

101 Splaying north-west from the DST is the Gilboa Fault, and farther north-west towards the Mediterranean,
102 the Carmel Fault. Both comprise an active zone generalized as the Carmel Fault Zone (CFZ). The DST segments
103 are capable of producing $M 6$ and $M 7-7.5$ events (Shamir et al., 2001; Hamiel et al., 2009), and the CFZ is capable
104 of producing up to $M 6.5$ earthquakes (Grünthal et al., 2009).

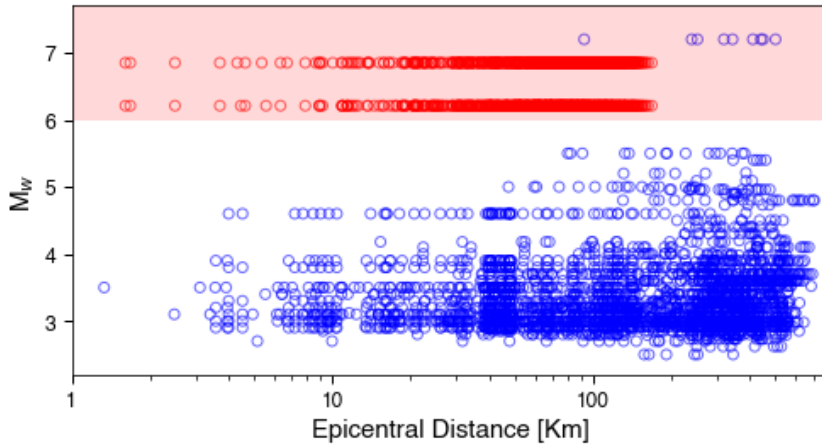
105 The Israel Seismic Network (ISN), established in 1983 and upgraded over the years, consists of a mixture
106 of different instrumental and operational stations, including short-period stations (14 in total), broadband stations
107 (24 in total), and a large broadband array (part of the Comprehensive Nuclear Test Ban Treaty). The deployment
108 of the ISN does not cover areas of increased seismic hazard, e.g., densely populated zones and soil sites, or areas
109 designated by the Israel Seismic Code (IS413) as suspected in extreme ground motion amplification, such as the
110 Zevulun Valley (Fig. 1b). Currently, the seismic network is upgraded within the TRUAA project (an early warning
111 system), with up to 69 strong-motion accelerometers and 12 broadband seismometers added to ISN (Kurzon et
112 al., 2020). However, most of the instrumentation are placed along the DST and Carmel fault to provide early
113 warning, and not in densely populated or industrialized areas where the seismic risk is tangible. Based on

114 demographic projections (the Taub Center for Social Policy Study in Israel; For URL see data and resources) the
 115 population of Israel is expected to grow from 9.05 million in 2021 to 12.8 million in 2040 and combined with the
 116 increasing demand for housing and infrastructures, the seismic risk is expected to grow.

117 The Israel seismic catalog covers 36 years of measurements (1985–2021) and includes more than 23,300
 118 events (Wetzler & Kurzon, 2016), but only 15 of them are of $M > 5$ (Fig. 1a and Fig. 2). Moving back in time,
 119 Israel's pre-instrumental catalog spans over 3000 years (Agnon, 2014; Zohar, 2019) with many catastrophic
 120 events, such as the 749 ($M > 7$), 1202, ($M > 7.5$), 1759 ($M > 7$), and the 1837 ($M > 7$) earthquakes, among others.
 121 In total, fourteen $M > 7$ events were cataloged by Ambraseys (2006) in the past two millennia. Recent geodetic
 122 studies (Hamiel et al., 2016; Sadeh et al., 2012) identified a slip deficit on specific segments of the DST, such as
 123 the Jordan Gorge Fault (JGF) and the Jordan Valley Fault (JVF), equivalent to an $M > 7$ earthquake.



124 **Figure 1.** (a) Israel Seismic catalog (M_w) for the period 1985-2021 orange circles are events with $M_w > 5$ (expansion of
 125 Wetzler & Kurzon (2016) catalog). Red lines are active tectonic borders and faults, DST is Dead Sea Transform, CFZ is
 126 Carmel Fault Zone. (b) Demographics of Israel and the Palestinian Authority (PA) and the deployment of the Israel Seismic
 127 Network. Yellow triangles are the old (up to October 2017) Israel Seismic network stations, brown triangles are the current
 128 (TRUAA) seismic network stations. (after Kurzon et al., (2020)). GS is Gaza Strip. The black rectangles define the
 129 computational domain presented in Fig. 3a.



130
 131 **Figure 2.** Israel's ground motion database (blue circles) for the period 1983-2021 as a function of epicentral distance (Yagoda-
 132 Biran et al., 2021). The shaded rectangle spans the $M_w > 6$ region of moderate-strong ground motion records. The red circles
 133 are the simulated ground motions from this work.

134 2.2 Spatial heterogeneity of Israel

135 The geological structure of Israel exhibits strong spatial heterogeneity over short scales (Fig. 3a,b). Deep pull-
 136 apart basins (up to 10 km) filled with soft sediments ($V_s \sim 600\text{-}800 \text{ m sec}^{-1}$) accompany the active DST system,
 137 from south to north: The Dead Sea Basin, Beit Shean Valley (BSV), the Sea of Galilee (SG) and the Hula Valley
 138 (Rosenthal et al., 2019). Along the CFZ, the Zevulun, Harod, and Jezreel Valleys are formed. The vulnerability
 139 of Zevulun Valley is particularly crucial because of its dense population and the high concentration of strategic
 140 industrial infrastructure (Shani-Kadmiel et al., 2020).

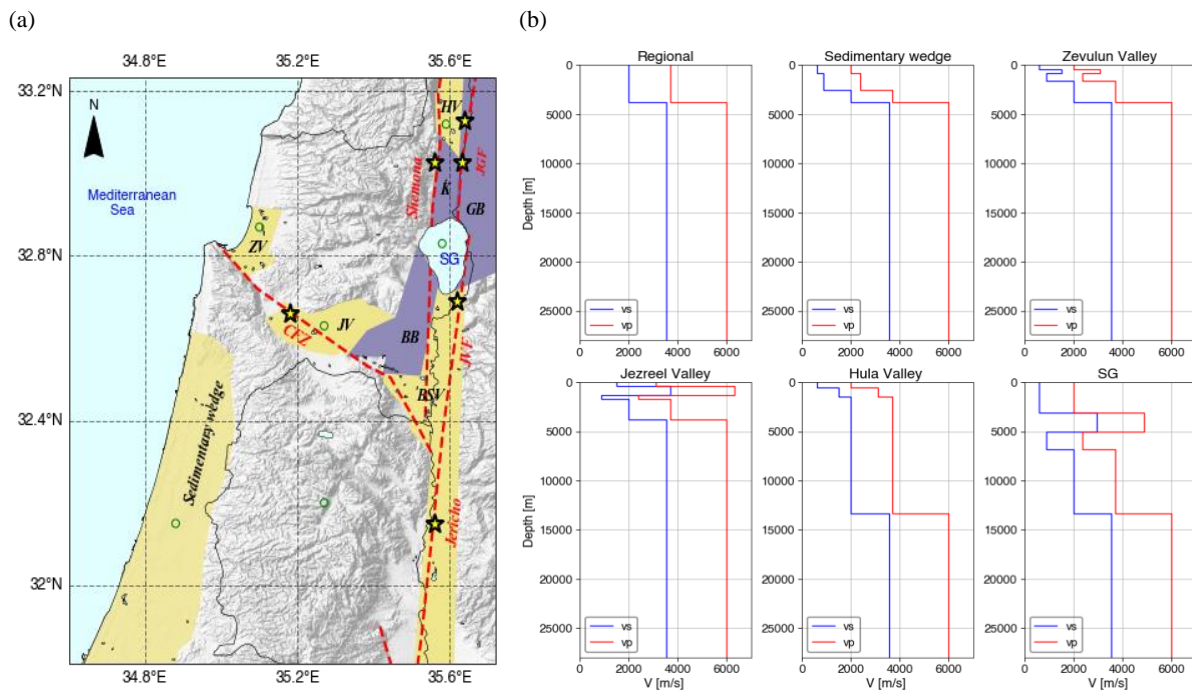
141 The Israeli coastal plain, one of the most densely populated regions of the country (on average, 9000 people
 142 per km^2), is underlain by a westward thickening sedimentary wedge (SW). In the Judea foothills area, east of the
 143 SW, a strong reflector exists between the sandstones and clays (Pleistocene Kurkar Gr, $V_s \sim 300 \text{ m sec}^{-1}$) and the
 144 hard carbonate rocks (the Cretaceous Judea Group, $V_s \sim 2000 \text{ m sec}^{-1}$). In the coastal plain, the Kurkar Group
 145 overlays the soft carbonates (Avedat Gr, $V_s \sim 900 \text{ m sec}^{-1}$) and clastic sediments (the Bet Guvrin Fm., $V_s \sim 800$
 146 m sec^{-1}) (refer to Fig. 3b). The depth of the Kurkar Group base reflector is typically several tens of meters. Further
 147 to the west, a prominent reflector is a contact between the clays (Pliocene Yafo Fm., $V_s \sim 600 \text{ m sec}^{-1}$) and top of
 148 Judea Group (Gvirtzman et al. 2008). These two reflectors, when shallower than 250 m, were used for the latest
 149 update of the Israel Building Code IS 413 (Israel Standards Institution, 2013) to delineate areas of high potential
 150 of ground motion amplification (Gvirtzman and Zaslavsky, 2009). This situation further complicates the process
 151 of developing an empirical GMM for Israel.

152 2.3 Source effects

153 The impact of inter-basin sources along the DST on regional ground motions was examined by Shimony et al.,
 154 (2021). This work clearly showed that regional ground motions are determined by source-path coupling effects in
 155 the strike-slip basins before waves propagate into the surrounding areas. Ground motions are determined by the
 156 location of the rupture nucleation, the near-rupture lithology, and the local structures. Shimony et al., focused on
 157 symmetric sub-shear ruptures and did not model rupture directivity or super-shear rupture velocities, both known
 158 to amplify regional ground motions.

159 Under specific conditions, super-shear ruptures and directivity occur on bi-material faults (Shi & Ben-Zion
 160 2006). Specifically, for subsonic propagation, symmetrically initiated bilateral rupture evolves after some
 161 propagation distance to a unilateral rupture in the positive direction, which is the direction of slip on the compliant
 162 side of the fault containing the softer layer. The magnitude of this effect increases with propagation velocity and
 163 the degree of material contrast across the fault. At super-shear propagation speeds, along a bi-material fault, the
 164 propagation direction is reversed.

165 The DST is a mature left-lateral fault with a 105 km offset, resulting in strong material contrast between
 166 the hard layers on the Jordan side (east) and the soft layers on the Israeli side (west). Thus, the rupture can
 167 potentially propagate unilaterally southwards, discharging most of the seismic energy into Israel or northward in
 168 super-shear mode. The Jordan Gorge Fault and the Jordan Valley Fault (both active faults of the DST) specifically
 169 can produce an earthquake with rupture propagating in super-shear velocity since they border deep sedimentary
 170 basins, characterized by large shear wave velocities contrast along the rupture propagation path. Thus, to quantify
 171 the seismic hazard ensuing from bi-material faults, it is necessary to study the two propagation directions; both
 172 sub-shear and super-shear velocities.



173 **Figure 3.** (a) The DST fault system and the Carmel Fault Zone (CFZ) and accompanying structures. Sedimentary structures
 174 (yellow): BSV-Beit Shean Valley, ZV-Zevulun Valley, JV-Jezreel Valley, HV-Hula Valley, SG-Sea of Galilee, and the
 175 Sedimentary wedge; and hard rock structures (purple): K-Korazim structural saddle, BB-Belvoir Basalts, GB-Golan Basalts.
 176 The yellow stars indicate the epicenter of the seismic sources simulated in our work: Jordan Gorge Fault (JGF), with bilateral
 177 and unilateral slip realization, Jordan Valley Fault (JVF), Jericho Fault, Shemona Fault (only for M 7), and CFZ (only for M
 178 6). (b) Representative depth velocity profiles of the computational domain (green circles).

179 3 Methodology and workflow

180 Developing a regional GMM for Israel requires a database of ground motion records, including $M > 6$ events at
181 short, <100 km, distances. To supplement the existing ground motions database, we added a suite of synthetic
182 ground motions from physics-based 3D numerical models of different $M 6$ and $M 7$ earthquakes (Fig. 2).

183 Our work comprised two main stages; first, we modified and expanded the regional velocity model of
184 Shimony et al., (2021), to represent a more realistic geological setting and contain the Golan Basalts, the central
185 part of Israel, and the sedimentary wedge. Then, we simulated five different earthquake scenarios for each
186 magnitude, with nucleation at different locations along the DST and CFZ. For each scenario, we recorded synthetic
187 ground motions at 129 stations (see supplementary material, Fig. S1), with 124 stations deployed in a uniform
188 grid with 10 km spacing and five more stations in areas of interest (such as Zevulun Valley, Kiryat Shemona,
189 among others). Next, we performed statistical analysis of the synthetic database, using multivariable regression,
190 by minimizing residuals between data and model estimations. We then formulated a parametric model of the
191 ground motions and examined the median ground motions and their variability for each of the simulated scenarios.

192 3.1 Numerical model

193 Ground motions in this research were modeled using the SW4v2 software (Petersson and Sjogreen, 2014, 2017a,
194 b), developed for large-scale simulations of seismic wave propagation on parallel computers.

195 The velocity model covers the northern and central part of Israel (fig. 4a) and includes the main DST trough
196 and the following basins/structures, from south to north: Beit Shean Valley (BSV), Belvoir Basalts (BB), Sea of
197 Galilee (SG), Korazim structural saddle (K), Golan Basalts (GB) and Hula Valley (HV). Along the CFZ, we model
198 the major sedimentary basins of Jezreel Valley (JV) and Zevulun Valley (ZV). The coastal plain is underlain by
199 the westward thickening Sedimentary wedge (SW). Geographically, the model extends from the city of Ashdod
200 in the south (31.8° N, 34.6° E) to Hula Valley in the north (33.23° N, 35.72° E) and from the Mediterranean Sea
201 in the west to the Golan Basalts in the east. Figures 4b,c,d illustrate the north-south and east-west cross-sections
202 of the velocity profiles. The numerical domain spans 159 km in the north-south direction and 124 km in the east-
203 west direction. It covers almost 80 % of the Israeli population and a significant part of the population of the
204 Palestinian Authority.

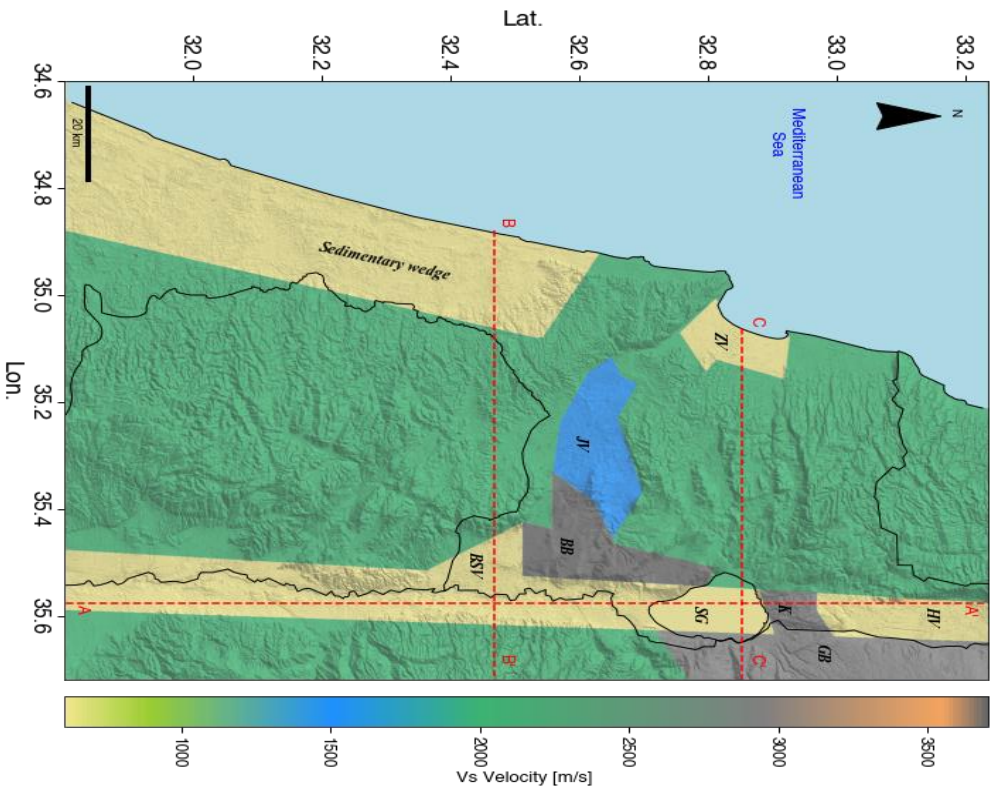
205 Subsurface geometry and the characteristics of the DST trough were obtained from Rosenthal et al., (2019)
206 with modifications for the Hula Valley, obtained from the density log of the Notera 3 (Rybakov et al., 2003). The
207 sedimentary wedge structure retrieved from Gvirtzman et al. (2008) and the Zevulun Valley structure was set
208 using data from Gvirtzman et al. (2011). The basement depth along the model is based on Ben-Avraham et al.,
209 (2002). Five physical quantities describe the viscoelastic material model used in this research: shear wave velocity
210 (V_s), pressure wave velocity (V_p), density (ρ), and seismic quality factors (Q_s , Q_p) for each point in the
211 computational space. The missing parameters were assessed indirectly by using the correlation presented by
212 Brocher (2008). The main units with their respective velocity, density and quality factors are shown in Table 1.

213 Seismic sources were modeled using the distributed slip model (DSM) developed by Shani-Kadmiel et al.,
214 (2016). DSM is a kinematic model which describes the rupture patch as an elliptic surface with maximum slip at
215 the nucleation point, decaying toward the edges as a pseudo-Gaussian function (Fig. S2). Shani-Kadmiel et al.,
216 (2016) present validation of the DSM using macroseismic reports of the 1927 Jericho earthquake, showing good
217 agreement between the reported and simulated ground motions. Rupture patch size and displacements were scaled

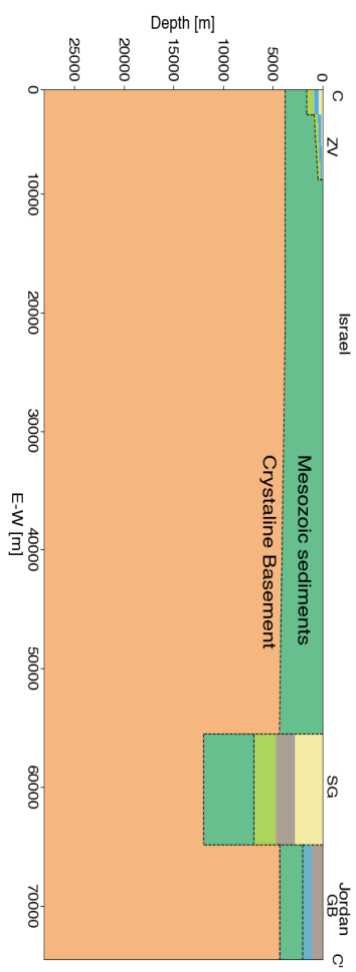
218 following the relations presented in Wells & Coppersmith (1994). All sources were modeled as left-lateral, vertical
219 strike slips (a dip of 90° and rake of 0°), with a strike of 3° for sources on the DST and a strike of 325° for the
220 CFZ. The moment-rate time function of each point on the rupture patch was set to a GaussianInt pulse (Pettersson
221 and Sjogreen, 2017b) with a central frequency of $f_0=0.4$ Hz and a maximum frequency of $f_{\max}=1$ Hz.

222 The depth of the model was set to 28 km corresponding to the maximum seismogenic depth in this region
223 (Wetzler and Kurzon, 2016). We assigned a minimum shear wave velocity of 608 m s^{-1} for the uppermost
224 sedimentary layer due to the computational limitations of our system. Grid spacing was set to 76 m in accordance
225 with the minimum shear wave velocity and the maximum frequency of the source. We set the simulation time to
226 120 seconds to allow the slowest waves to propagate across the entire computational domain. The main parameters
227 of the numerical setting are summarized in Table 2.

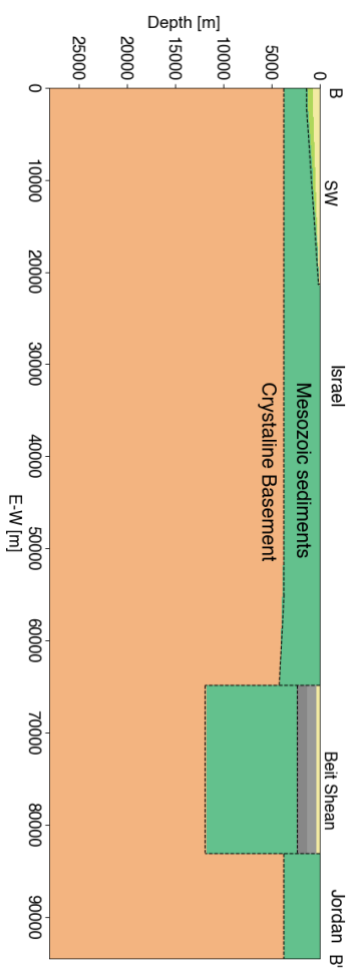
(a)



(b)



(c)



(d)

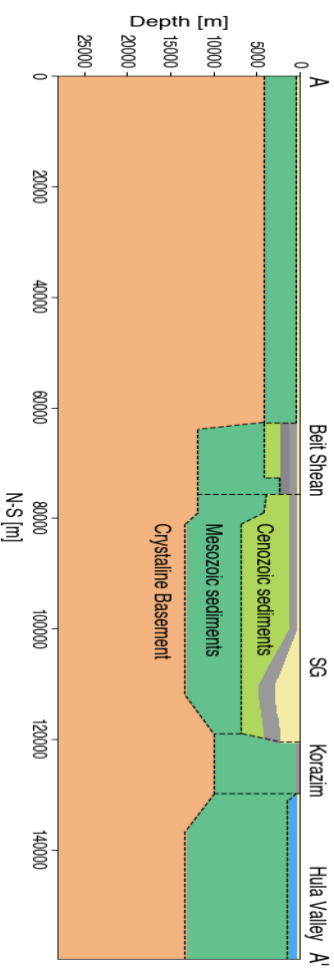


Figure 4. (a) The numerical model of the computational domain accompanied with subsurface cross-sections, marked with red dashed lines: (b) east-west cross section through Zevulun Valley, CC' (c) east-west cross-section through the Sedimentary wedge, BB' and (d) north-south cross-section through the DST trough, AA'.

Table 1. Material properties of main stratigraphic units used in this work

Model part	Rock Formation	Vs [m s ⁻¹]	Vp [m s ⁻¹]	Qs	Qp	ρ [Kg m ⁻³]
Regional	Crystalline basement	3550	6000	403	806	2720
	Cenozoic and Mesozoic sediments (Judea/ Talme Yafe, Mount Scopus Avedat, and Lower Saqiye)	2000	3700	160	320	2350
Local variations:						
DST	Cenozoic sediments (Umm Sabune, Bira and Gesher)	887	2380	62	124	2054
	Miocene volcanics (lower basalt)	3698	6330	439.5	879	2790
	Pliocene volcanics (upper basalt)	2947	4900	282	564	2520
	Notera/Lisan	608	2000	39.87	79.74	1900
Hula	Cenozoic sediments	1500	3100	111.5	223	2245
	Notera/Lisan	608	2000	39.87	79.74	1900
JV	Cenozoic sediments (Umm Sabune, Bira, and Gesher)	887	2380	62	124	2054
	Miocene volcanics (lower basalt)	3698	6330	439.5	879	2790
	Cenozoic sediments	1500	3100	111.5	223	2245
ZV	Cenozoic and Senonian sediments (Mount Scopus Avedat and Beit Guvrin)	887	2380	62	124	2054
	Cenozoic sediments (Patish)	1500	3100	111.5	223	2245
	Cenozoic sediments (Kurkar and Yafo)	608	2000	39.87	79.74	1900
SW	Cenozoic sediments (Lower Saqiye)	887	2380	62	124	2054
	Cenozoic sediments (Kurkar and Upper Saqiye)	608	2000	39.87	79.74	1900

Table 2. Main parameters of the numerical model

Parameters	Value
Model Dimensions (L×W×D)	159.63 Km × 124.45 Km × 28 Km
Spatial spacing (dh)	76 m
Grid size (points)	1.27×10^9
Time step spacing	0.0125 s
Simulated time	120 s
Source Dimensions (L×D)	M 6: 32 Km × 15 Km M 7: 38 Km × 22 Km
Source maximum and average slip	M 6: 0.5 and 0.2 m M 7: 3 and 1.57 m
Seismic moment (M_0)	M 6: 2.57×10^{18} N·m (Mw 6.21) M 7: 2.37×10^{19} N·m (Mw 6.85)
Source fundamental (f_0) and maximal frequencies (f_{max})	0.4 and 1 Hz

3.2 Earthquake scenarios and database

To examine the variability of ground motions from moderate M 6 and strong M 7 earthquakes, we concentrated

on earthquake events nucleating on active segments of the DST system, with known slip deficit, and along the

234 CFZ. We modeled a symmetric bilateral rupture on the Jordan Gorge Fault (JGF-B), Jericho Fault (JF) Carmel
 235 Fault Zone (CFZ) and the Shemona Fault (SF), a southward unilateral rupture on the JGF (JGF-U), and a super-
 236 shear rupture on the Jordan Valley Fault (JVF) (Fig. 3).

237 The hypocenter for the DST events was placed in the middle of the seismogenic depth; 11 and 13 Km, for
 238 the M 6 and M 7 respectively, for the M 6 CFZ, the value was set to 12 Km. The rupture patch was designed to
 239 be contained in uniform lithology to prevent super-shear rupture speeds in the shallow parts of our model.
 240 Therefore, rupture speed for each scenario was set to $0.9 V_S$ of the lithology surrounding the nucleation zone. The
 241 only exception was the JVF scenario for both M 6 and M 7, in which we modeled super-shear effects. For this
 242 scenario, the rupture nucleates within the hard rock with a sub-shear speed of 1800 m s^{-1} and evolves into
 243 supershear rupture when it ruptures the sediments with shear wave velocity of $<900 \text{ m s}^{-1}$. The rupture velocity of
 244 each scenario corresponds to the local variations of the sediment's depth. Following the transition of the nucleation
 245 zone from the shallow crystalline basement in the south and west parts of the model to the thick Mesozoic and
 246 Cenozoic sediments in the north and the east, the rupture velocity decreases from 3195 m s^{-1} along the Shemona,
 247 Carmel, and Jericho faults to 1800 m s^{-1} along the JGF and JVF faults. As a reference, we simulated a simple two-
 248 layered reference model (Ref) on the JGF, with mechanical properties similar to the regional setting, following
 249 Aldersons et al., (2003). The scenarios are summarized in Table 3.

250 **Table 3.** Earthquake scenarios

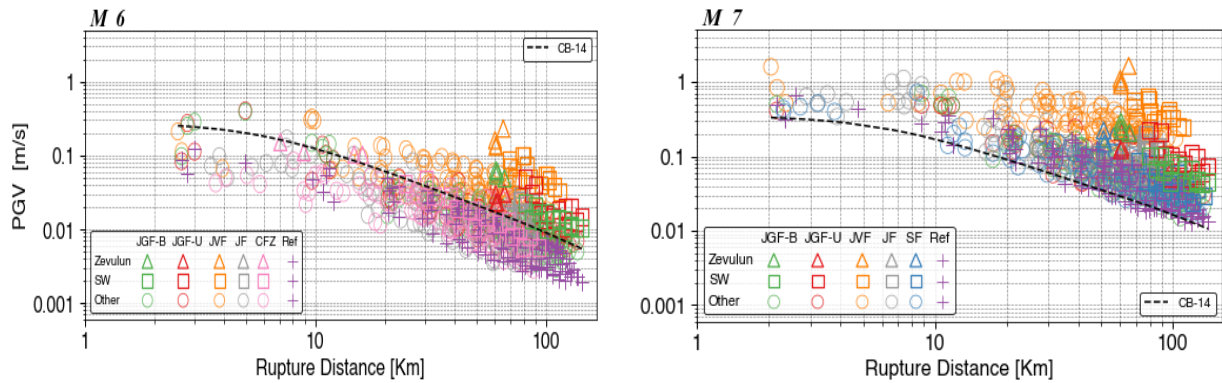
Fault Name	Scenario	Magnitude (M)	Rupture speed (m s^{-1})	Hypocentral depth (Km)
Jordan Gorge	Bilateral rupture (JGF-B)	6, 7	1800	11 and 13
Jordan Gorge	Southward unilateral rupture (JGF-U)	6, 7	1800	11 and 13
Jordan Valley	Bilateral super-shear rupture (JVF)	6, 7	1800	11 and 13
Jericho	Bilateral rupture (JF)	6, 7	3195	11 and 13
Shemona	Bilateral rupture (SF)	7	3195	13
Carmel	Bilateral rupture (CFZ)	6	3195	12
Reference	Bilateral rupture (Ref)	6, 7	3195	11 and 13

251 **4 Results**

252 In this section, we report the simulation results and the simulation-based attenuation model for M 6 and M 7. We
 253 begin with elaborating on the regression process and its deliverable, the attenuation model. Next, we present the
 254 ground motions variability, starting from total and following with within-event, and between-event PGV
 255 residuals, and the contribution of each earthquake scenario to the total deviation. Then, we proceed with looking
 256 into single station variability, through maps of the predicted and simulated PGV, with the corresponding residuals
 257 at each station. Finally, we show the PGV and the 5 %- 95 % ground motions significant duration (D_s 595)
 258 correspondence between predicted by global GMM's (CB14, Afshari & Stewart, 2016, respectively) and
 259 simulated.

260 4.1 Simulation results

261 For each simulation, we attained a set of 129 synthetic ground motion records (3 components each; N-S, E-W,
 262 and vertical) from the network deployed in the computational domain. Next, we calculated the PGV values for
 263 each scenario at each station as the maximum value over the three components. We decided to exclude some of
 264 the M 7 near-source records (stations: 104,105 and 106 for the JVF scenario and stations: 122,123 and 129 for the
 265 JGF-B, JGF-U, and Shemona scenarios) due to high strain values and possible non-linear effects, not compatible
 266 with the linearity assumption of our model. In total, our ground motions database consists of 645 and 633 synthetic
 267 records for M 6 and M 7, respectively. Figure 5 presents our results in terms of PGV as a function of distance. We
 268 used different markers for records from the sedimentary structures of the Zevulun Valley and the Sedimentary
 269 wedge to differentiate them from the remaining data.



270 **Figure 5.** Simulation results, PGV-distance space, for bilateral rupture on the Jordan Gorge Fault (JGF-B), Jericho Fault (JF)
 271 Carmel Fault Zone (CFZ; for M 6) and the Shemona Fault (SF; for M 7), a southward unilateral rupture on the JGF (JGF-U),
 272 and a super-shear rupture on the Jordan Valley Fault (JVF); for M 6 (left) and M 7 (right). The records from Zevulun Valley
 273 and the Sedimentary wedge (SW) are marked with triangles and rectangles, respectively. The other records are marked
 274 with circles; the reference records are marked with pluses. For comparison, the CB14 is plotted for a strike-slip fault,
 275 $Z_{2.5}=0.42$ Km and $V_{S30}=1686$ m s⁻¹ (representing averaged values over all the sites).

276 4.2 Statistical analysis of ground motions results

277 The next step was to formulate a parametric ground motion attenuation model (AM) for the two magnitudes based
 278 on our simulations. Such a model will provide an estimate for the median ground motions and their variability.
 279 The general parametric form of the AM for both M 6 and M 7 is based on the CB14 function and presented in Eq.
 280 (1):

$$281 \ln Y = a \ln \left(\sqrt{R_{RUP}^2 + b} \right) + c \ln \left(\frac{V_{s,surf}}{V_{s,ref}} \right) + d Z_2 + e \pm \sigma \quad (1)$$

282 Where Y is ground motion intensity measure (IM). Due to the bandwidth of our numerical models (0.1 to 1 Hz),
 283 we formulated the AM in terms of PGV. We used the closest distance to the fault rupture plane (R_{RUP} as defined
 284 in CB14) as the initial explanatory variable. To improve the accuracy of the model, we incorporated two additional
 285 variables into the regressions: surface shear wave velocity at the site ($V_{s,surf}$) and the depth to $V_S = 2$ km s⁻¹ (Z_2),
 286 which is the depth to the hard Mesozoic sediments (top Judea Group) considered the primary reflector in the
 287 region. a , b , c , d , and e are model coefficients, and σ is the standard deviation. The $V_{s,ref}$ is the shear wave velocity
 288 corresponding to the Judea Group in the computational domain, which in our model equals 2000 m s⁻¹.

289 The process of minimizing the residuals as a function of each explanatory variable can be found in the
 290 supplementary material (Fig. S3). We used $V_{S, \text{surf}}$ instead of the more common V_{S30} , as our grid resolution is 76
 291 m, preventing us from accurately determining the time-averaged shear wave velocity in the top 30 m of each site
 292 in our model. The coefficients and the total standard deviation for each model are summarized in Table 4.

293 **Table 4.** Regression coefficients for the attenuation model (AM)

Mag.	IM	a	b	c	d		e		Standard Deviation (σ)
					$R_{\text{rup} > 58 \text{ km}}$ and $z_2 > 0$	$R_{\text{rup} < 58 \text{ km}}$ or $z_2 = 0$	$R_{\text{rup} > 58 \text{ km}}$ and $z_2 > 0$	$R_{\text{rup} < 58 \text{ km}}$ or $z_2 = 0$	
6	PGV	-1.01	59.34	-0.685	0		0.56		0.6
7	PGV	-1.22	151.81	-0.669	0.56	0	2.08	2.42	0.629

294 4.3 AM Variability

295 We then examined the simulated data and the contribution of each scenario to the AM variability. We calculated
 296 the within-event (δW) and between-event (δB) residuals (see Al Atik et al., (2010)) for each magnitude and
 297 distance:

$$298 \delta W_{i,j} = \ln \text{PGV}_{i,j}^{\text{sim}} - \ln \text{PGV}_i^{\text{m}} \quad (2)$$

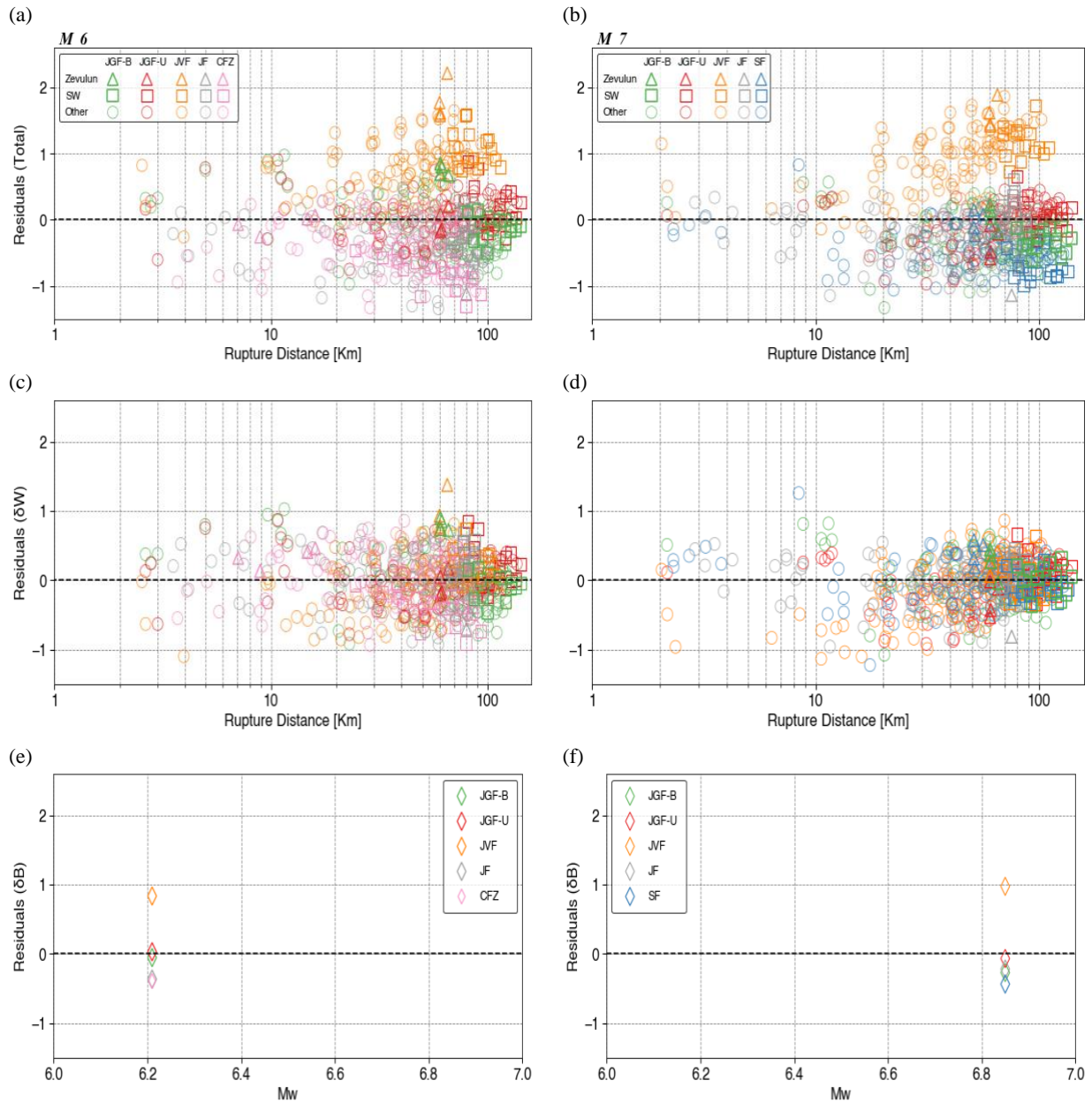
$$299 \delta B_i = \ln \text{PGV}_i^{\text{m}} - \ln \text{PGV}^{\text{AM}} \quad (3)$$

300 where $\text{PGV}_{i,j}^{\text{sim}}$ is the simulation value for event i and recording j , PGV_i^{m} is the median for event i , and PGV^{AM} is
 301 the AM median value. The total residual is the sum of the within and between event residuals.

302 The residuals are presented in Fig. 6: total (Fig. 6a and 6b), within-event (Fig. 6c and 6d), and between-
 303 events (Fig. 6e and 6f). The total residuals (Fig. 6a and 6b) show a large underprediction of the PGV from the
 304 JVF scenario (orange) on which we modeled a super-shear rupture, up to a ratio of 2.5 and 2 in the Zevulun Valley
 305 (orange triangles), for M 6 and M 7, respectively. However, the AM also exhibits over predictions; The PGV from
 306 the scenarios nucleated in the crystalline basement (SF, JF, and CFZ), with rupture speed= 3195 m s^{-1} , are
 307 overpredicted down to a ratio of more than -1 (in ln units).

308 Some within-event residuals exhibit distance dependency; for M 7, the JVF (super-shear) and JGF-U
 309 (directivity model) residuals increase with rupture distances greater than 20 km. The JVF residuals also
 310 demonstrate the same distance dependency for M 6; however, the effect is less prominent when compared to M7.

311 The effect of the rupture directivity (JGF-U) is demonstrated in comparing the Zevulun Valley and the
 312 Sedimentary wedge within-event residuals (Fig. 6c and 6d). While in a symmetric rupture (JGF-B), the seismic
 313 energy dissipates equally into the north and south parts of the model, in an asymmetric rupture (JGF-U), more
 314 energy propagates toward the south, resulting in stronger ground motions at the Sedimentary wedge (Fig. 5).
 315 However, the ground motions are less intensive at the Zevulun Valley compared to the symmetric rupture. As a
 316 result, the within-event residuals for Zevulun Valley are higher for the JGF-B scenario compared to the JGF-U
 317 scenario, while for the Sedimentary wedge, the opposite is true. Most clearly, the JVF between-event residuals
 318 are the highest for both M 6 and M 7 with a ratio of 1 (Fig. 6e, and 6f).



319 **Figure 6.** Residuals between simulated and attenuation model (AM) PGV as a function of rupture distance (R_{RUP}), for bilateral
 320 rupture on the Jordan Gorge Fault (JGF-B), Jericho Fault (JF) Carmel Fault Zone (CFZ; for M 6) and the Shemona Fault (SF;
 321 for M 7), a southward unilateral rupture on the JGF (JGF-U), and a super-shear rupture on the Jordan Valley Fault (JVF); for
 322 M 6 (left) and M 7 (right); (a) and (b) total residuals, (c) and (d) within-event (δW) residuals, (e) and (f) between-event (δB)
 323 residuals. The records from Zevulun Valley and the Sedimentary wedge (SW) are marked with triangles and rectangles,
 324 respectively. The other records are marked with circles. Residuals are in ln units.

325 We further studied the single station variation of ground motions and quantified the misfit between the
 326 simulated PGV and the AM PGV. We calculated the mean ground motion and its standard deviation at each
 327 station. The residuals for single station k were calculated as follows:

328
$$\delta_k = \ln PGV_k^{sim} - \ln PGV_k^{AM} \quad (4)$$

329 where PGV_k^{sim} and PGV_k^{AM} are the simulated and predicted mean PGV at station k, respectively. Figure 7 and
330 Figure 8 show the mean simulated and mean AM PGVs for M 6 and M 7, respectively. For each station, we also
331 plotted the standard deviation using a scaled diameter circle.

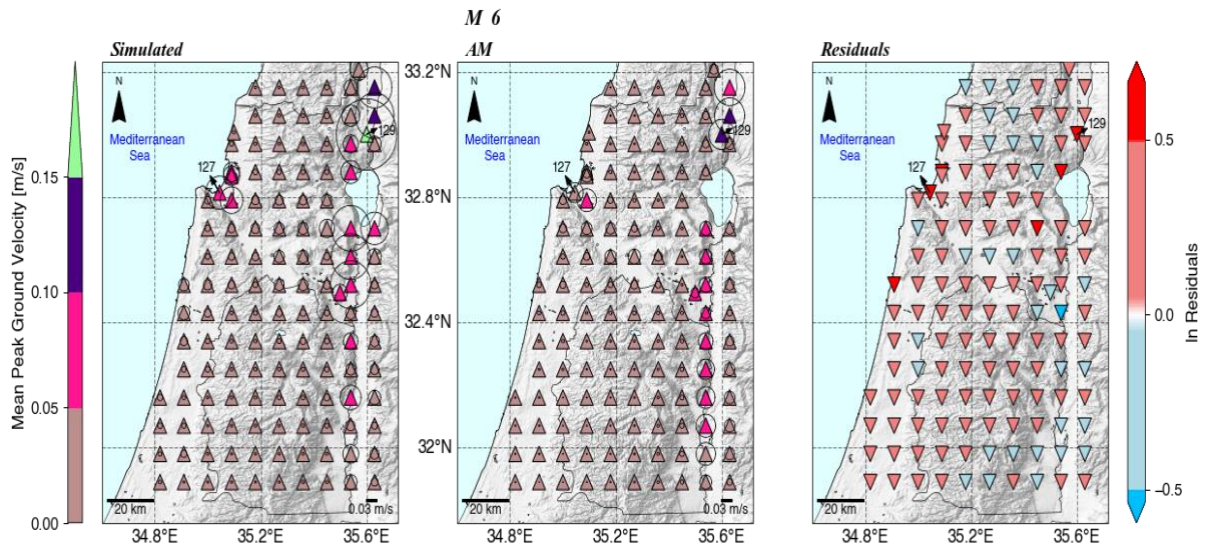
332 Both figures show that simulated ground motions variability at a single station is large, not fully covered
333 by the AM. For example, simulated ground motions at station 129 located on the Hula Valley exhibit a significant
334 standard deviation. For M 6, it is the largest value (green triangle) of 0.17 m s^{-1} compared to 0.09 m s^{-1} (indigo)
335 predicted by the AM, while for M 7, the largest standard deviation is 0.59 m s^{-1} (orange triangle) compared to
336 0.02 m s^{-1} (light green triangle) observed at station 127 located on the Zevulun Valley. As a result, there is a large
337 discrepancy between the simulated and AM values at specific stations.

338 In general, as expected from normal log distribution, higher mean PGV values are accompanied by a
339 larger standard deviation for both magnitudes. It is of significance for seismic hazard assessment, as outlier
340 ground motions at specific sites, mainly from $M < 7$ earthquakes, could be a significant source of damage
341 (Minson et al., 2020)

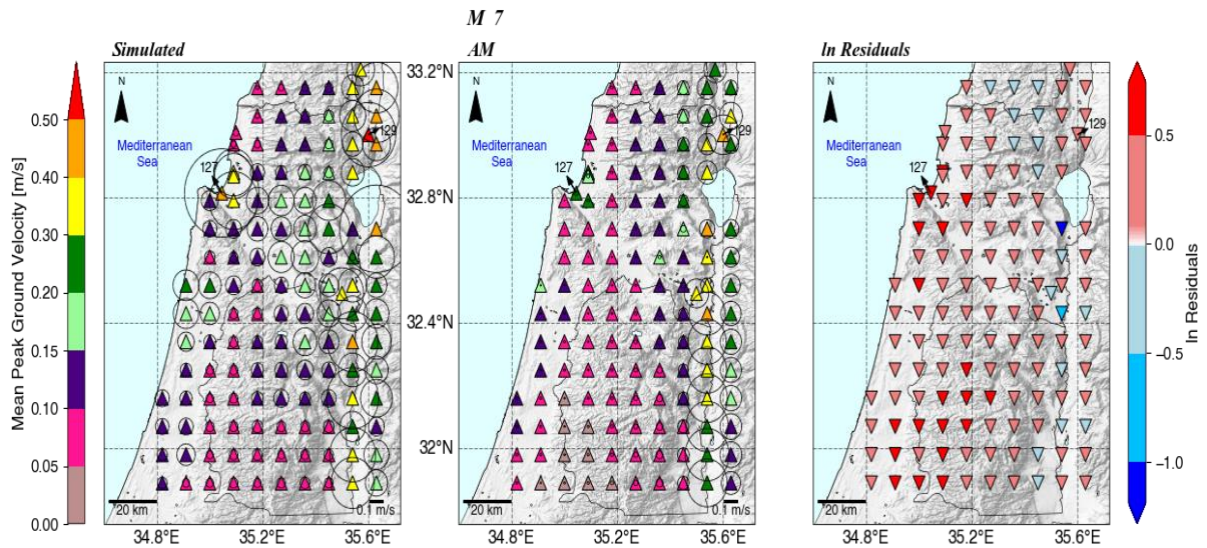
342 4.4 Comparison with global models

343 To examine the agreement between our simulations with an instrumental, global GMM, we calculated the total
344 residuals between PGVs from our simulations and PGVs predicted by the CB14 model. We chose the CB14 model
345 as it is planned to supersede the CB08 model used in the Israel Building Code (413). The CB14 PGVs were
346 calculated for a strike-slip fault, where we used the surface shear wave velocity as the V_{s30} parameter and the basin
347 response term Z_2 as $Z_{2.5}$. Figure 9 shows the total residuals for the AM and CB14 models as a function of distance
348 (R_{RUP}). For both magnitudes, the AM (mean and standard deviation) oscillates near the zero-model bias (black
349 horizontal dotted line). However, it deviates when approaching the region containing rupture distances typical of
350 the Zevulun Valley. The effect is more noticeable for M 7. Figure 9 also shows that the CB14 is less consistent
351 and performs differently for each magnitude. While for M 6, the GMM mostly over predicts (negative values) the
352 simulated PGV (until reaching ZV and SW rupture distances zones), for M 7, it mostly under predicts them
353 (positive values), except for large distances, up to a factor of 2 and above. In addition, the residuals calculated
354 with respect to CB14 exhibit a significant standard deviation of the mean ground motion, with considerably larger
355 variability for M 7.

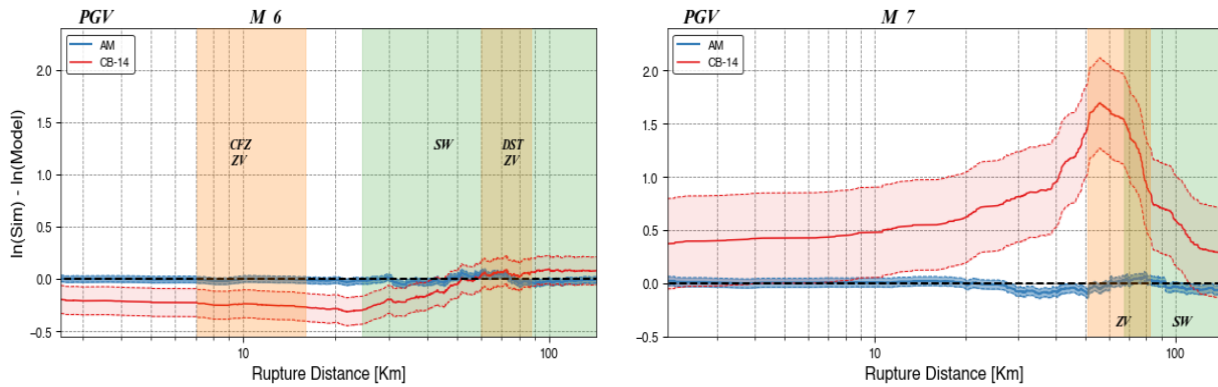
356 It is important to note that, by averaging the PGVs, we subdue the performance of both models at individual
357 stations/Rupture distances; thus, we cannot analyze the residual's spatial variations at a specific location.
358 However, it is sufficient to demonstrate that the global model deviates considerably from simulated ground
359 motions.



360 **Figure 7.** Map view of simulated and AM mean PGV (triangles) for M 6 and their standard deviation (diameter of the circles)
 361 at each station, with the respective residuals in ln units (inverted triangles).



362 **Figure 8.** Map view of simulated and AM mean PGV (triangles) for M 7 and their standard deviation (diameters of the circles)
 363 at each station, with the respective residuals in ln units (inverted triangles).

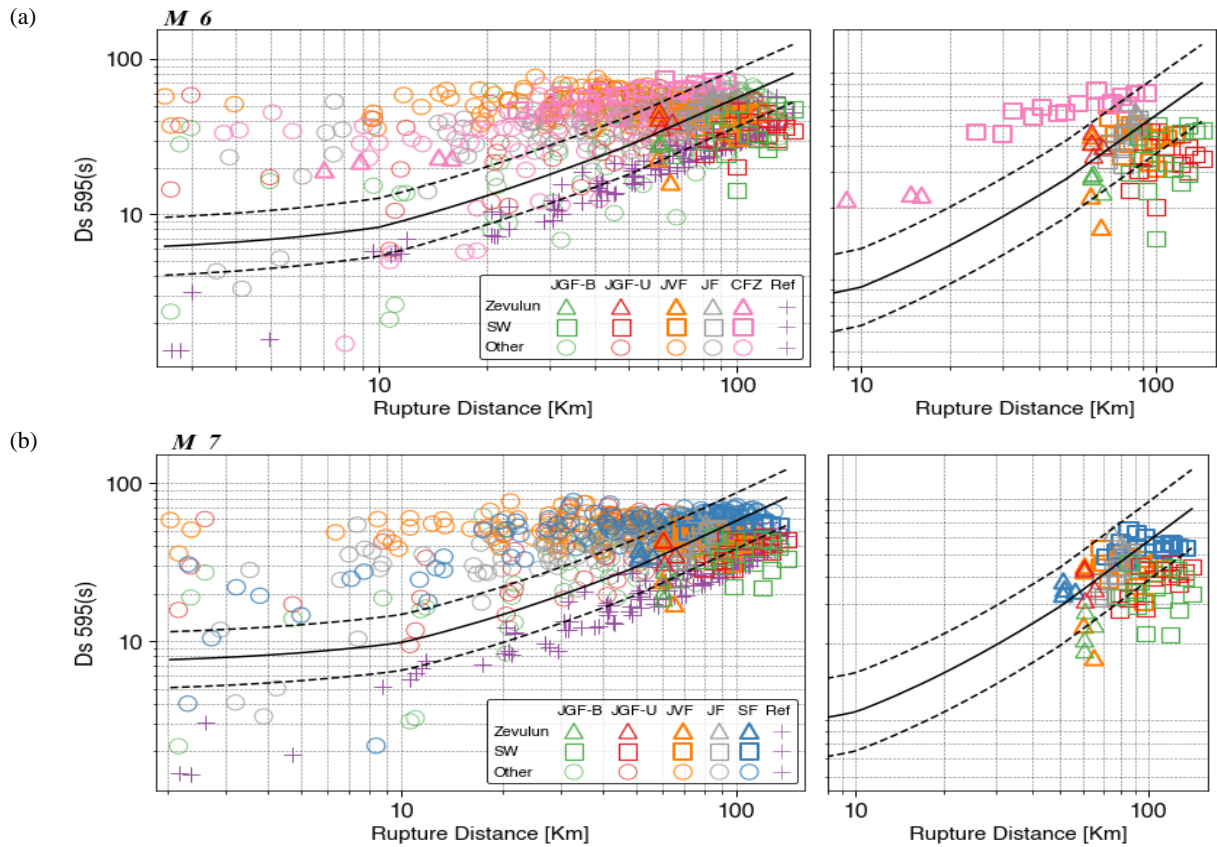


364 **Figure 9.** PGV Residuals between simulated (Sim) and predicted by the AM (blue) and CB14 (red) models, as a function of
 365 rupture distance (R_{RUP}), for M 6 (left) and M 7 (right). Thick lines represent the mean, and the shaded region denotes the
 366 standard deviation at each distance. The green and yellow shaded regions indicate the range of rupture distances related to the
 367 Sedimentary wedge (SW) and the Zevulun Valley (ZV), respectively. Residuals are in ln units.

368 4.5 Significant duration

369 Another important intensity measure is the significant duration ($D_s 595$), the time interval between 5 % to 95 %
 370 of the cumulative seismic energy (Arias Intensity) at a site. Figure 10 shows the simulated and empirical $D_s 595$
 371 values as a function of rupture distance. The typical increase of the empirical model with distance is captured in
 372 the reference (laterally homogenous) model. However, for all other models, the significant duration remains nearly
 373 constant, at ruptures distances larger than 20 km. In addition, the empirical GMM mostly under-predicts the
 374 simulated values between 2 to 50 Km for both magnitudes.

375 We postulate that this is caused by the complex geological setting of our model. The impact of geological
 376 complexity is reflected in $D_s 595$ values from near-source stations, Zevulun Valley (triangles), and the
 377 Sedimentary wedge (rectangles). At near-source stations, the significant duration is large due to the effects of deep
 378 sedimentary structures along the DST, which also prolongs the path duration of the ground motions in other sites
 379 (Shimony et al., 2021), resulting in long significant duration with almost no path dependency. On the contrary at
 380 the Zevulun Valley and the SW, the energy accumulates faster than in other sites, as the ground motions are
 381 amplified, reaching 95 % of the total energy over a shorter duration. Interestingly, the significant duration in
 382 Zevulun Valley is lower than in the Sedimentary wedge. As we expect from deep sedimentary structures to
 383 prolong shaking duration, it may sound counterintuitive. However, it is explained by the relative proximity of the
 384 Zevulun Valley to the rupture. Whereas in Zevulun Valley, most of the energy arrives as a pulse at the beginning
 385 of the record, the energy at the more distant Sedimentary wedge accumulates more gradually and reaches its
 386 maximum almost at the end of the record, resulting in longer $D_s 595$ values. In general, there is no large deviation
 387 between the simulated significant duration for M 6 and M 7. However, the empirical model shows a longer
 388 duration for M 7. This resembles in source duration is related to the DSM settings, more specifically to the source
 389 fundamental frequency, which in our study, is the same for both magnitudes; and it is a subject for testing in future
 390 works.



391 **Figure 10.** 5 % to 95 % ground motions significant duration ($D_s 595$) comparison between simulated and empirical GMM
 392 (Afshari and Stewart, 2016), for bilateral rupture on the Jordan Gorge Fault (JGF-B), Jericho Fault (JF) Carmel Fault Zone
 393 (CFZ; for M 6) and the Shemona Fault (SF; for M 7), a southward unilateral rupture on the JGF (JGF-U), and a super-shear
 394 rupture on the Jordan Valley Fault (JVF); for M 6 (a) and M 7 (b). Main plots (left) accompanied with subplots showing only
 395 the records from the Zevulun Valley and the Sedimentary wedge (right). Solid and dashed lines represent the median and the
 396 standard deviation of the empirical GMM, respectively. The records from Zevulun Valley and the Sedimentary wedge (SW)
 397 are marked with triangles and rectangles, respectively. The other records are marked with circles.

398 5 Discussion and Summary

399 A strong earthquake in Israel is imminent. However, up to date, a comprehensive regional GMM describing the
 400 spatial variability of ground motions has not yet been developed. This is mainly due to low seismicity rates and
 401 magnitude bounded strong motion database, coupled with sparse instrumental coverage. The current ground
 402 motion database lacks events with magnitude $M > 6$. To examine different source and path effects on ground
 403 motions variability, we simulated M 6 and M 7 earthquakes with different source and path properties.
 404 Subsequently, to study the ground motions variability, we developed a parametric attenuation model (AM) of
 405 PGV for M 6 and M 7 earthquakes, based on R_{RUP} , Z_2 , and $V_{s, surf}$ explanatory values.

406 Our analysis showed that the AM was unable to fully capture the variability of the simulated ground
 407 motions. Except for the Jordan Valley Fault (JVF) scenarios, the AM overestimates most of the modeled ground
 408 motions. We postulate that this overestimation results from the outlier, higher PGV values from the JVF scenario
 409 (Fig. 5), shifting the average ground motion toward them. Also, the within-event residuals for the JVF scenario
 410 show a distance dependency for $R_{RUP} > 20$ Km, continuing to grow away from the fault. We describe this scenario

411 as a "black swan" of our simulations and account its outlier behavior to the effects of the super-shear rupture,
412 specific to this model, affecting both the source (between-event residuals) and path (within-event residuals) terms
413 of the ground motions (Fig.6). Super-shear ruptures behave differently from sub-shear ruptures in many aspects.
414 Most pertinent to our analysis is the slow energy decay of the super-shears relative to sub-shears (Bhat et al.,
415 2007); thus, it cannot be fully captured by our AM, which is based mainly on sub-shear ruptures. In addition, it
416 was found that Z_2 , depth to Mesozoic rock, has a very small impact (<0.001) on the standard deviation for the M
417 6, reducing it from 0.5998 to 0.5988 (Fig. S3). As a result, the M 6 model depends only on rupture distance and
418 $V_{s, surf}$. For M 7, Z_2 is a good predictor for soil sites ($Z_2 > 0$) located >58 Km from the source, including the Zevulun
419 Valley and the Sedimentary wedge (Fig. 6d), imposing a great seismic hazard. We do not see a clear dependence
420 of the deep sedimentary structures with Z_2 , along the DST. We speculate that Their site response may be masked
421 by nearby source effects and requires additional analysis.

422 For each scenario, both magnitudes considered, we observed high PGV values at the Zevulun Valley and
423 the Sedimentary wedge associated with local site effects. These sedimentary structures exhibit a larger
424 discrepancy between the simulated and AM PGV values when compared with other sites. Such deviation indicates
425 that the AM does not fully capture the site effects of these complex structures, and future model refinements are
426 required. Likewise, the single station variability shows that the simulated values' highest mean and standard
427 deviation were in Zevulun Valley and near-source stations. In addition, a relatively high standard deviation was
428 also found in the Sedimentary wedge for M 7. This large single station variability is, apparently, the impact of the
429 outlier JVF PGV values. The AM does not account for the standard deviation at near-source and Zevulun Valley
430 stations for the M 6 and almost at all stations for the M 7. In fact, as the AM was unable to capture the simulated
431 JVF PGV values, it is expected that the single station variability cannot be captured either. Furthermore, the larger
432 discrepancy for M 7 is due to the larger deviation of the JVFs ground motions from those of sub-shear ruptures
433 (Fig. 5), on which the AM is mainly based.

434 Noteworthy to mention is that while the effect of the super-shear rupture on the AM performance is
435 systematic over the entire computational domain, comprised of both source and path effects (Fig.6), the effect of
436 the southward directivity is distance-dependent, path effect, increasing towards the south, related to a larger
437 amount of energy discharged in this direction. Additional records of super-shear and directivity ruptures and
438 accounting for these source effects by additional model terms will improve the performance of the AM and will
439 assist in better understanding the implications of these phenomena on the seismic hazard in Israel.

440 The comparison of the simulated ground motions with a global GMM (CB14) showed that this model is
441 not well constrained for the simulated ground motions and does not capture their total variability. We note that
442 the comparison was performed on a single IM, the PGV values, one of several intensity measures provided by the
443 CB14. Thus, our findings are pertinent to the variability of PGV solely. It should be noted that PGV is a good
444 proxy for structural damage (e.g., to Kaestli & Fäh, (2006); Wald et al., (1999)), hence a crucial parameter for
445 seismic hazard mitigation. This discrepancy between modeled PGV and CB14 PGVs will inevitably result in a
446 discrepancy in the evaluation of structural damage.

447 The significant duration (D_s 595) comparison showed again that the imported model performs differently
448 than the simulated ground motion and cannot explain the local variability due to complex geological structure,
449 affecting the source, path, and site terms of the ground motions, such as the path independence of the significant
450 duration. However, we note that the D_s 595 from our simulations were calculated based on low frequency content

451 (<1Hz) and may be biased from Ds 595 calculated based on the complete spectrum comprised of both low and
452 high frequencies. The effects of the frequency content on significant duration may be a potential topic for research
453 in future works.

454 Regional simulations of near-fault ground motions from large Mw 7 earthquakes in Lebanon, based on a
455 1-D velocity approximation, were presented by Fayjaloun et al., (2021). A comparison between the results
456 reported by Fayjaloun et al., (2021) with our results is somewhat limited. Specifically, it was shown that structural
457 and material heterogeneity of the crust in Israel results in regional ground motions variability (Volk et al., 2017;
458 Shani-Kadmiel et al., 2020; Shimony et al., 2021). These effects could only be captured by 3-D modeling.

459 We acknowledge that our AM is not independent of the evaluated models, thus describing both their
460 explanatory and predictive power (Mak et al., 2017). However, our goal was not to develop an independent and
461 comprehensive GMM but to study the ground motion variability through a parametric model.

462 Recently, Maiti et al., (2021) developed a suite of nine GMMs for Israel, in the magnitude range of 3 to 8
463 and distance range of 1 to 300 Km. These models are formulated in Fourier amplitude spectra (FAS) and are based
464 on one empirical and four simulated ground motion datasets and two empirical host models. The simulated ground
465 motions were generated using the Stochastic Method SIMulation (SMSIM) model of Boore (2003), with a unique
466 set of parameters for each simulation, calibrated with the empirical ground motions dataset (discussed in detail in
467 Yagoda-Biran et al., (2021)). However, the GMMs do not fully account for a local source, path, and site effects
468 due to sparse empirical database at large magnitudes ($M > 6$) and the utilization of a point-source stochastic
469 simulation method. This method is useful for simulating mean ground motions. Yet, it is less appropriate for
470 simulating site-specific and earthquake-specific ground motions and low-frequency ground motions, which are
471 affected by the 3D geometry of the computational domain. The AM presented in this work is based on 3D
472 simulations and incorporates a finite fault source with different rupture properties. This is the first step toward
473 developing a regional GMM, accounting for local source, path, and site effects. In subsequent work, which is
474 beyond the scope of the current research, we intend to develop a complete GMM for Israel, which will include all
475 the magnitudes and will be based on empirical ($M < 6$) as well as on synthetic ($M > 6$) databases. In addition, we
476 plan to incorporate new path and site terms such as $Z_{0.8}$ for the Zevulun valley and the Sedimentary wedge,
477 distance-dependent and rupture velocity-dependent attenuation for Directivity and super-shear ruptures, among
478 others; as well as a source term for super-shear ruptures. Such a model is expected to perform better than imported
479 global models by maintaining both; a lower aleatory variability and, as new synthetic data will be added to the
480 database, reduced epistemic uncertainty of the median ground motions (Abrahamson et al., 2019).

481 The population of Israel is fast-growing, with an annual rate of 1.8 % (OECD 2020 data), compared with
482 the 0.4 % average of the OECD. Coupled with fast economic growth of 4.5 % (OECD 2019 data), the demand for
483 housing and infrastructure constantly elevates the seismic risk in Israel. Our work shows that the ground motions
484 in Israel from M 6 and M 7 earthquakes are expected to be very damaging, up to 8-9 EMS (Fig. S4). Furthermore,
485 the modeled ground motions exhibit considerable spatial variability, which imported GMMs do not fully capture.
486 The development of a local comprehensive GMM model is therefore critical for the mitigation of seismic risk. In
487 the foreseen future, the moderate-strong ground motion data gap will be filled by synthetic ground motion records
488 from systematic numerical simulations.

489 **Data and resources**

490 Israel Seismic catalog (Fig. 1a), expanded after Wetzler & Kurzon (2016) catalog and the configuration of the
491 Israel seismic network (Fig. 1b) after Kurzon et al., (2020) can be found at
492 <https://earthquake.co.il/en/earthquake/searchEQS.php> and <https://earthquake.co.il/en/network/accNetwork.php>,
493 respectively. The ground motions database of Israel (Fig. 2) discussed in Yagoda-Biran et al., (2021) is available
494 at <https://earthquake.co.il/en/hazards/EngSeismology.php>. The Taub Center population projections for Israel are
495 accessible at <https://www.taubcenter.org.il/en/pr/population-projections-for-israel-2017-2040/>. OECD population
496 and economic growth rates can be found at <https://data.oecd.org/israel.htm#profile-economy>. Simulations were
497 performed using SW4 version 2.0 (v2.0; Petersson and Sjögreen, 2017a), an open-source package for wave
498 propagation simulations, available at github.com/geodynamics/sw4 (last accessed June 2021). Data processing
499 was done with the pySW4 package from Shahr Shani-Kadmiel, available at
500 <https://github.com/shaharkadmiel/pySW4> (last accessed July 2021), and "obspsy" (Beyreuther et al., 2010),
501 developed for numerical seismology. Figures were prepared with Matplotlib (Hunter, 2007) and Cartopy (Met
502 Office, 2016). Peak ground velocity (PGV) values, according to Campbell and Bozorgnia (2014), were calculated
503 using the Next Generation Attenuation-West Project (NGA-West2) ground-motion prediction equations (GMPEs)
504 excel file, available at <https://apps.peer.berkeley.edu/ngawest2/databases/> (last accessed July 2021). The
505 supplemental material includes: (1) synthetic station network deployed in our models (Fig. S1); (2) distributed
506 slip model (DSM) slip distribution and rupture time (Fig. S2); (3) the evolution of the residuals between simulated
507 and attenuation model (AM) PGV for M 6 and M 7 (Fig. S3) and (4) map view of simulated mean EMS intensity
508 calculated according to Kaestli & Fäh, (2006).

509 *Competing interests.* The authors declare that they have no conflict of interest.

510 **Acknowledgments**

511 This research was partially funded by the Ministry of Energy, Israel (Grant Number 219-17-02). Co-author JG
512 was partially supported by the Ministry of Energy scholarship for graduate studies (Tender 76/19).

513 **References**

- 514 Abrahamson, N. A., Kuehn, N. M., Walling, M., and Landwehr, N.: Probabilistic seismic hazard analysis in
515 california using nonergodic ground-motion models, *Bull. Seismol. Soc. Am.*, 109, 1235–1249,
516 <https://doi.org/10.1785/0120190030>, 2019.
- 517 Afshari, K. and Stewart, J. P.: Physically parameterized prediction equations for significant duration in active
518 crustal regions, *Earthq. Spectra*, 32, 2057–2081, <https://doi.org/10.1193/063015EQS106M>, 2016.
- 519 Agnon, A.: Pre-instrumental earthquakes along the Dead Sea rift, in: *Modern Approaches in Solid Earth*
520 *Sciences*, vol. 6, Springer, 207–261, https://doi.org/10.1007/978-94-017-8872-4_8, 2014.
- 521 Aldersons, F., Ben-Avraham, Z., Hofstetter, A., Kissling, E., and Al-Yazjeen, T.: Lower-crustal strength under
522 the Dead Sea basin from local earthquake data and rheological modeling, *Earth Planet. Sci. Lett.*, 214, 129–142,
523 [https://doi.org/10.1016/S0012-821X\(03\)00381-9](https://doi.org/10.1016/S0012-821X(03)00381-9), 2003.
- 524 Ambraseys, N. N.: Comparison of frequency of occurrence of earthquakes with slip rates from long-term

525 seismicity data: The cases of Gulf of Corinth, Sea of Marmara and Dead Sea Fault Zone, *Geophys. J. Int.*, 165,
526 516–526, <https://doi.org/10.1111/j.1365-246X.2006.02858.x>, 2006.

527 Anderson, J. G. and Brune, J. N.: Probabilistic seismic hazard analysis without the ergodic assumption, *Seismol.*
528 *Res. Lett.*, 70, 19–28, <https://doi.org/10.1785/gssrl.70.1.19>, 1999.

529 Al Atik, L., Abrahamson, N., Bommer, J. J., Scherbaum, F., Cotton, F., and Kuehn, N.: The variability of
530 ground-motion prediction models and its components, *Seismol. Res. Lett.*, 81, 794–801,
531 <https://doi.org/10.1785/gssrl.81.5.794>, 2010.

532 Bartov, Y., Steinitz, G., Eyal, M., and Eyal, Y.: Sinistral movement along the Gulf of Aqaba - Its age and
533 relation to the opening of the Red Sea, *Nature*, 285, 220–222, <https://doi.org/10.1038/285220a0>, 1980.

534 Ben-Avraham, Z., Ginzburg, A., Makris, J., and Eppelbaum, L.: Crustal structure of the Levant Basin, eastern
535 Mediterranean, 346, 23–43, [https://doi.org/10.1016/S0040-1951\(01\)00226-8](https://doi.org/10.1016/S0040-1951(01)00226-8), 2002.

536 Beyreuther, M., Barsch, R., Krischer, L., Megies, T., Behr, Y., and Wassermann, J.: ObsPy: A python toolbox
537 for seismology, *Seismol. Res. Lett.*, 81, 530–533, <https://doi.org/10.1785/gssrl.81.3.530>, 2010.

538 Bhat, H. S., Dmowska, R., King, G. C. P., Klinger, Y., and Rice, J. R.: Off-fault damage patterns due to
539 supershear ruptures with application to the 2001 Mw 8.1 Kokoxili (Kunlun) Tibet earthquake, *J. Geophys. Res.*
540 *Solid Earth*, 112, 1–19, <https://doi.org/10.1029/2006JB004425>, 2007.

541 Boore, D. M.: Simulation of ground motion using the stochastic method, *Pure Appl. Geophys.*, 160, 635–676,
542 <https://doi.org/10.1007/PL00012553>, 2003.

543 Brocher, T. M.: Key elements of regional seismic velocity models for long period ground motion simulations, *J.*
544 *Seismol.*, 12, 217–221, <https://doi.org/10.1007/s10950-007-9061-3>, 2008.

545 Campbell, K. W. and Bozorgnia, Y.: NGA ground motion model for the geometric mean horizontal component
546 of PGA, PGV, PGD and 5% damped linear elastic response spectra for periods ranging from 0.01 to 10 s,
547 *Earthq. Spectra*, 24, 139–171, <https://doi.org/10.1193/1.2857546>, 2008.

548 Campbell, K. W. and Bozorgnia, Y.: NGA-West2 ground motion model for the average horizontal components
549 of PGA, PGV, and 5% damped linear acceleration response spectra, *Earthq. Spectra*, 30, 1087–1114,
550 <https://doi.org/10.1193/062913EQS175M>, 2014.

551 Chaljub, E., Moczo, P., Tsuno, S., Bard, P. Y., Kristek, J., Käser, M., Stupazzini, M., and Kristekova, M.:
552 Quantitative comparison of four numerical predictions of 3D ground motion in the Grenoble Valley, France,
553 *Bull. Seismol. Soc. Am.*, 100, 1427–1455, <https://doi.org/10.1785/0120090052>, 2010.

554 Douglas, J. and Aochi, H.: A survey of techniques for predicting earthquake ground motions for engineering
555 purposes, *Surv. Geophys.*, 29, 187–220, <https://doi.org/10.1007/s10712-008-9046-y>, 2008.

556 Fayjaloun, R., Dabaghi, M., Cornou, C., Causse, M., Lu, Y., Stehly, L., Voisin, C., and Mariscal, A.: Hybrid
557 Simulation of Near-Fault Ground Motion for a Potential Mw 7 Earthquake in Lebanon, *Bull. Seismol. Soc. Am.*,
558 111, 2441–2462, <https://doi.org/10.1785/0120210091>, 2021.

559 Garfunkel, Z.: Lateral motion and deformation along the Dead Sea transform, in: *Modern Approaches in Solid*
560 *Earth Sciences*, vol. 6, Springer International Publishing, 109–150, https://doi.org/10.1007/978-94-017-8872-4_5, 2014.

562 Graves, R. and Pitarka, A.: Refinements to the Graves and Pitarka (2010) broadband ground-motion simulation
563 method, *Seismol. Res. Lett.*, 86, 75–80, <https://doi.org/10.1785/0220140101>, 2015.

564 Graves, R., Jordan, T. H., Callaghan, S., Deelman, E., Field, E., Juve, G., Kesselman, C., Maechling, P., Mehta,

565 G., Milner, K., Okaya, D., Small, P., and Vahi, K.: CyberShake: A Physics-Based Seismic Hazard Model for
566 Southern California, *Pure Appl. Geophys.*, 168, 367–381, <https://doi.org/10.1007/s00024-010-0161-6>, 2011.

567 Grünthal, G., Hakimhashemi, A., Schelle, H., Bosse, C., and Wahlström, R.: The long-term temporal behaviour
568 of the seismicity of the Dead Sea Fault Zone and its implication for time-dependent seismic hazard assessments,
569 <https://doi.org/10.2312/GFZ.b103-09098>, 2009.

570 Gvirtzman, Z., Zilberman, E., and Folkman, Y.: Reactivation of the Levant passive margin during the late
571 Tertiary and formation of the Jaffa Basin offshore central Israel, *J. Geol. Soc. London.*, 165, 563–578,
572 <https://doi.org/10.1144/0016-76492006-200>, 2008.

573 Gvirtzman Z., I. M. and Sagee, Y.: Re-processing and geological re-interpretation of old seismic lines of Haifa
574 bay, *Geol. Surv. Isr. GSI/27/2011*, 2011.

575 Gvitzman, Z. and Zaslavsky, Y.: Map of Zones with Potentially High Ground Motion Amplification:
576 Explanatory Notes, Rep. Num. GSI/15/2009, 2009.

577 Hamiel, Y., Amit, R., Begin, Z. B., Marco, S., Katz, O., Salamon, A., Zilberman, E., and Porat, N.: The
578 seismicity along the dead sea fault during the last 60,000 years, *Bull. Seismol. Soc. Am.*, 99, 2020–2026,
579 <https://doi.org/10.1785/0120080218>, 2009.

580 Hamiel, Y., Piatibratova, O., and Mizrahi, Y.: Creep along the northern Jordan Valley section of the Dead Sea
581 Fault, *Geophys. Res. Lett.*, 43, 2494–2501, <https://doi.org/10.1002/2016GL067913>, 2016.

582 Hunter, J. D.: Matplotlib: A 2D graphics environment, *Comput. Sci. Eng.*, 9, 90–95,
583 <https://doi.org/10.1109/MCSE.2007.55>, 2007.

584 Israel Standards Institution: Standard SI 413. Design Provisions for Earthquake Resistance of Structures.
585 Amendment No. 5, 2013.

586 Kaestli, P. and Fäh, D.: Rapid estimation of macroseismic effects and Shakemaps using macroseismic data, in:
587 1st European Conf. Earthquake Engineering and Seismology, 1535, 2006.

588 Kuehn, N. M., Abrahamson, N. A., and Walling, M. A.: Incorporating nonergodic path effects into the NGA-
589 west2 ground-motion prediction equations, *Bull. Seismol. Soc. Am.*, 109, 575–585,
590 <https://doi.org/10.1785/0120180260>, 2019.

591 Kurzon, I., Nof, R. N., Laporte, M., Lutzky, H., Polozov, A., Zakosky, D., Shulman, H., Goldenberg, A.,
592 Tatham, B., and Hamiel, Y.: The “TRUAA” seismic network: Upgrading the Israel Seismic Network-toward
593 national earthquake early warning system, *Seismol. Res. Lett.*, 91, 3236–3255,
594 <https://doi.org/10.1785/0220200169>, 2020.

595 Lan, X., Xing, H., Zhou, J., and Zhao, J. X.: A comparison of the source, path, and site effects of the strong-
596 motion records from the western and the southwestern parts of China with modern ground-motion prediction
597 equations, *Bull. Seismol. Soc. Am.*, 109, 2691–2709, <https://doi.org/10.1785/0120180293>, 2019.

598 Maiti, S. K., Yagoda-Biran, G., and Kamai, R.: A Suite of Alternative Ground-Motion Models (GMMs) for
599 Israel, *Bull. Seismol. Soc. Am.*, 111, 2177–2194, <https://doi.org/10.1785/0120210003>, 2021.

600 Mak, S., Cotton, F., and Schorlemmer, D.: Measuring the performance of ground-motion models: The
601 importance of being independent, <https://doi.org/10.1785/0220170097>, 2017.

602 Met Office: Cartopy: a cartographic python library with a matplotlib interface, <http://scitools.org.uk/cartopy>,
603 2016.

604 Minson, S. E., Baltay, A. S., Cochran, E. S., McBride, S. K., and Milner, K. R.: Shaking is almost always a

605 surprise: The earthquakes that produce significant ground motion, *Seismol. Res. Lett.*, 92, 460–468,
606 <https://doi.org/10.1785/0220200165>, 2020.

607 Mizutori, M. and D’ebarati, G.: The human cost of disasters: an overview of the last 20 years (2000-2019), UN
608 Off. Disaster Risk Reduction., <https://doi.org/10.18356/79b92774-en>, 2020.

609 Pesaresi, M., Ehrlich, D., Kemper, T., Siragusa, A., Florczyk, A., Freire, S., and Corbane, C.: Atlas of the
610 Human Planet 2017. Global Exposure to Natural Hazards. EUR 28556 EN, 92 pp., 2017.

611 Petersson, N. A. and Sjogreen, B.: SW4 Users Guide, Lawrence Livermore Natl. Lab. Tech. Rep. LLNL-SM,
612 662014, 2014.

613 Petersson, N. A. and Sjogreen, B.: SW4, version 2.0, Computational Infrastructure of Geodynamics,
614 <https://doi.org/10.5281/zenodo.1045297>, 2017a.

615 Petersson, N. A. and Sjogreen, B.: User’s guide to SW4, version 2.0, LLNL-SM-741439., [https://doi.org/.](https://doi.org/),
616 2017b.

617 Pitarka, A., Akinci, A., De Gori, P., and Buttinelli, M.: Deterministic 3D Ground-Motion Simulations (0–5 Hz)
618 and Surface Topography Effects of the 30 October 2016 Mw 6.5 Norcia, Italy, *Earthquake, Bull. Seismol. Soc.*
619 *Am.*, <https://doi.org/10.1785/0120210133>, 2021.

620 Rosenthal, M., Ben-Avraham, Z., and Schattner, U.: Almost a sharp cut – A case study of the cross point
621 between a continental transform and a rift, based on 3D gravity modeling, 761, 46–64,
622 <https://doi.org/10.1016/j.tecto.2019.04.012>, 2019.

623 Rybakov, M., Fleischer, L., and ten Brink, U.: The Hula Valley subsurface structure inferred from gravity data,
624 *Isr. J. Earth Sci.*, 52, 113–122, <https://doi.org/10.1560/WF6V-4BVG-GXQM-PKVR>, 2003.

625 Sadeh, M., Hamiel, Y., Ziv, A., Bock, Y., Fang, P., and Wdowinski, S.: Crustal deformation along the Dead Sea
626 Transform and the Carmel Fault inferred from 12 years of GPS measurements, *J. Geophys. Res. Solid Earth*,
627 117, <https://doi.org/10.1029/2012JB009241>, 2012.

628 Shamir, G., Bartov, Y., Sneh, A., Fleisher, L., Arad, V., and Rosensaft, M.: Preliminary seismic zonation in
629 Israel, *earthquake.co.il*28 , pp., 2001.

630 Shani-Kadmie, S., Tsesarsky, M., and Gvirtzman, Z.: Distributed slip model for forward modeling strong
631 Earthquakes, *Bull. Seismol. Soc. Am.*, 106, 93–103, <https://doi.org/10.1785/0120150102>, 2016.

632 Shani-Kadmiel, S., Volk, O., Gvirtzman, Z., and Tsesarsky, M.: Ground motion amplification atop the complex
633 sedimentary basin of Haifa Bay (Israel), *Bull. Earthq. Eng.*, 18, 821–836, [https://doi.org/10.1007/s10518-018-](https://doi.org/10.1007/s10518-018-00533-9)
634 00533-9, 2020.

635 Shi, Z. and Ben-Zion, Y.: Dynamic rupture on a bimaterial interface governed by slip-weakening friction,
636 *Geophys. J. Int.*, 165, 469–484, <https://doi.org/10.1111/j.1365-246X.2006.02853.x>, 2006.

637 Shimony, R., Gvirtzman, Z., and Tsesarsky, M.: Seismic energy release from intra-basin sources along the dead
638 sea transform and its influence on regional ground motions, *Bull. Seismol. Soc. Am.*, 111, 295–308,
639 <https://doi.org/10.1785/0120200215>, 2021.

640 Volk, O., Shani-Kadmiel, S., Gvirtzman, Z., and Tsesarsky, M.: 3D effects of sedimentary wedges and
641 subsurface canyons: Ground-motion amplification in the Israeli coastal plain, *Bull. Seismol. Soc. Am.*, 107,
642 1324–1335, <https://doi.org/10.1785/0120160349>, 2017.

643 Wald, D. J., Quitoriano, V., Heaton, T. H., and Kanamori, H.: Relationships between peak ground acceleration,
644 peak ground velocity, and modified mercalli intensity in California, *Earthq. Spectra*, 15, 557–564,

645 <https://doi.org/10.1193/1.1586058>, 1999.

646 Walling, M. . and Abrahamson, N. .: Non-Ergodic Probabilistic Seismic Hazard Analyses, in: 15th World
647 Conference on Earthquake Engineering (15WCEE). Lisbon, Portugal, 24-28 September, 2012.

648 Wang, Z.: A Clear Definition of Seismic Hazard and Risk: A Basis for Hazard and Risk Assessment,
649 Communication, and Management, Am. Geophys. Union, 2005, S53B-1110, 2005.

650 Wells, D. L. and Coppersmith, K. J.: New empirical relationships among magnitude, rupture length, rupture
651 width, rupture area, and surface displacement, Bull. - Seismol. Soc. Am., 84, 974–1002, 1994.

652 Wetzler, N. and Kurzon, I.: The earthquake activity of Israel: Revisiting 30 years of local and regional seismic
653 records along the dead sea transform, Seismol. Res. Lett., 87, 47–58, <https://doi.org/10.1785/0220150157>, 2016.

654 Yagoda-Biran, G., Maiti, S. K., Wetzler, N., Nof, R. N., Pashcur, Y., and Kamai, R.: A ground-motion database
655 for Israel with its corresponding point-source parameters, for engineering seismology applications, Seismol.
656 Res. Lett., 92, 2679–2690, <https://doi.org/10.1785/0220200477>, 2021.

657 Zohar, M.: Temporal and spatial patterns of seismic activity associated with the Dead Sea transform (DST)
658 during the past 3000 yr, Seismol. Res. Lett., 91, 207–221, <https://doi.org/10.1785/0220190124>, 2019.

659